energies

MDPI

Article

Backpressure Supercompensation in a Novel Electrically Assisted Turbo Compound

Andrea Colletto *, Mirko Baratta and Daniela Anna Misul *

Department of Energy (DENERG), Politecnico di Torino, Corso Duca degli Abruzzi 24, 10129 Torino, Italy; mirko.baratta@polito.it
* Correspondence: andrea.colletto@studenti.polito.it (A.C.); daniela.misul@polito.it (D.A.M.)

Abstract

In the current environmental and political scenario, hybrid vehicles play crucial roles in the transition to sustainable mobility. The role of internal combustion engines (ICEs) is also of utmost importance to comply with the even more stringent emissions regulations. To that end, also considering the need for increased power density in ICEs, turbocharging allows for improved performance and reduced emissions. Within this context, the present paper introduces the novelties of a patented turbo compound layout with supercharging capabilities, i.e., the Turbo Generator Electric Multistage Supercharger (TGEMS) system. The analysis also allowed for providing evidence of a "backpressure supercompensation effect" associated with rising exhaust backpressure in the ICE. TGEMS introduces a novel compressor group decoupled from the turbine. The analyses were carried out on a 2.0 L turbocharged gasoline direct injection engine. The "supercompensation" phenomenon was isolated using a stepwise procedure in which TGEMS was initially applied to the baseline engine to be exploited on a modified configuration featuring a downscaled turbine. The results were analyzed from the perspectives of specific fuel consumption reduction and total power output as well as operating flexibility increase. The results indicate that, in a context like TGEMS, the assumption that rising exhaust backpressure is always penalizing is no longer valid. Under higher backpressure conditions, TGEMS alone achieved −4.92% in specific fuel consumption at 5000 rpm, with +8.75% in maximum power output. Moreover, with the configuration with a downscaled turbine and the possibility to control the engine operating line, specific fuel consumption reductions of −7.93% at 5000 rpm and −6.83% at 3000 rpm were achieved. The maximum power output increment was +11.04%. These outcomes could open up to new downsizing perspectives and a new generation of "super-backpressured engines".

Keywords: Hybrid Electric Vehicle (HEV); waste heat recovery; turbo compound; electric turbo compounding; Gasoline Direct Injection (GDI) engine; exhaust backpressure; fuel economy; brake power increase; efficiency; ICE operating line control

Check for updates

Academic Editors: Hubert Kuszewski and Paweł Woś

Received: 14 March 2026
Revised: 24 April 2026
Accepted: 26 April 2026
Published: 30 April 2026

1. Introduction

Today, hybrid vehicles play an increasingly crucial role in the development of sustainable mobility [1,2] by supporting the unavoidable need for the electric transition. Thanks to the availability of new technologies and recent research progress, even the most deeply rooted design criteria and the most consolidated technologies may need an overhaul, with the key objective of maximizing efficiency.

An example is turbo compound (TC) technology. Although it was considered a very promising solution for several decades [3–6], its application in the passenger car sector today plays a marginal role [1,4,6–10]. Originally developed in mechanical form (M-TC) [3,4,8,11–13], the advent of the hybrid vehicle era opened the door to electrifying the power turbine (PT) output, creating the electric turbo compound (E-TC) and electrically assisted turbo compound (eA-TC) categories [1,6–9,11,14,15].

But research on these categories seems to be carried out in a "classical" way, focusing only on "direct" benefits from the internal combustion engine (ICE) power output side, treating the ICE as the center point of the system, and targeting a "direct" reduction in brake-specific fuel consumption (*bsfc*) without degrading ICE performance [1,6,7,12,16,17]. This can be considered the primary reason that, by following this philosophy and its resulting paradigms, the most significant results and improvements have been achieved predominantly under high-load conditions [4,8–10]. This approach has led to TC applications generally focused on:

- very large displacement ICEs [1,4,6–10,13],
- hypersport vehicles [8,9,14].

1.1. The Turbo Compound

Today, this technology is divided into three macro-categories. Figure 1 displays a qualitative schematization of each system.

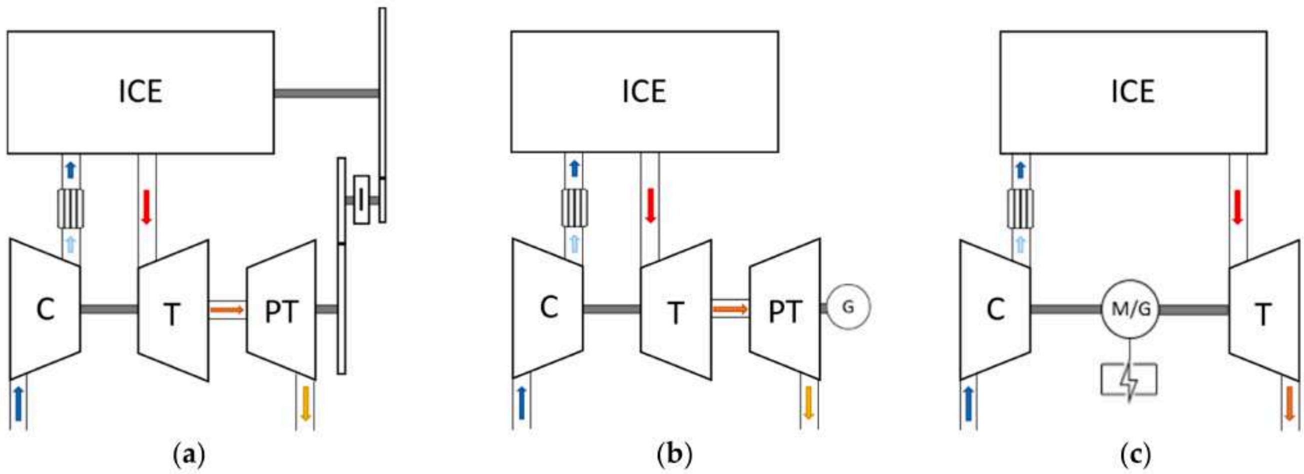

Figure 1. Different Turbo Compound layouts: (**a**) M-TC, (**b**) E-TC, (**c**) eA-TC.

In the previous classification, the PT connection typology was voluntarily simplified. However, it should be noted that the connection between the turbocharger turbine (T) and PT can be implemented in series or in parallel, with distinct advantages and drawbacks depending on the chosen configuration.

Generally, in a series configuration, the PT intercepts all exhaust gases exiting from T, so the PT must be operated under low-pressure conditions [6,7,10,12,17]. In a parallel configuration, the PT is installed on the exhaust line of the wastegate valve, which is before the T stage [6,7,10]. On the one hand, the series layout allows exploitation of the residual energy content of all exhaust gases, but on the other hand this condition is not trivial because the efficiency of conventional components is extremely low under low expansion ratio conditions, and exhaust backpressure tends to increase due to the presence of the stage [6,7,10,18,19]. Instead, in the parallel layout, on the one hand the PT can operate at a much higher expansion ratio and the engine sees lower exhaust backpressure, but on the other hand the amount of exhaust gases that can pass through the stage is limited, reducing recovery possibilities [6,7,10,19].

Overall, E-TC and eA-TC appear decidedly more suitable in situations where versatility and flexibility are required, such as in light-duty vehicles and passenger cars, because the PT or T is connected to an electric machine [1,6–9,11,14,15]. Their power-on-demand capability, high flexibility, and relatively low implementation costs make these solutions convenient, especially for hybrid vehicle development [1,6–9,14,15,18], in which recovered energy can be stored until it is needed.

Recent research applications demonstrate benefits in small-displacement gasoline or diesel engines, but the main advantages are concentrated at high load, with several drawbacks, such as an increase in *bsfc* at low load [4,6,9].

Given the real operating range of light-duty vehicles and passenger cars, it is clear that these technologies, which yield similar results, are generally not worth investing in for large-scale production.

1.2. The Backpressure Paradigm and the TGEMS System

Previously, the "classical" way to carry out the research has been mentioned. It refers to the role that the ICE plays within these power unit (PU) contexts and the way in which turbo matching is performed with the TC components. It is well known and considered obvious that, in an ICE, the engine exhaust backpressure should always be minimized, because otherwise there would be a degradation of ICE performance; this is an essential and basic rule, and it is reported in famous manuals, such as the Giancarlo Ferrari [20] (pp. 200–203). This assumption will be considered in this research as the Backpressure Paradigm.

The paradigm seems to have influenced all research in the TC field from the outset, with PT modified, enlarged, and redesigned [6,7,10,13,18,19,21] to minimize backpressure effects. However, the idea of the Backpressure Paradigm as a general constraint stems from the boundary conditions commonly present across all ICE operating conditions. Usually, when exhaust backpressure inside the manifolds increases, for example, by downsizing the T stage in a turbocharger, its negative effect cannot be compensated for by other components. The higher T energy cannot be exploited, and ICE performance, including *bsfc* [20] (pp. 200–203), will be negatively compromised.

In this research, this will be considered true not in the general domain but only in this specific application domain. If components capable of compensating for the effects of the backpressure increase are present in the system, the conclusion of the Backpressure Paradigm will be considered no longer valid.

More specifically, being in the TC field, the approach used in this article considers the ICE not only as a device that produces work but also as a volumetric burner that delivers high-temperature, high-pressure gases to the PT; analogous to a turbogas system [22–24]. The goal is to move part of the chemical energy fuel exploitation outside the engine cylinder, conducting it in a more efficient way without degrading ICE performance. But how does it maintain ICE performance?

In this way, to improve efficiency and to fulfill the increasingly stringent emission-reduction targets of the European Union [2], the Turbo Generator Electric Multistage Supercharger (TGEMS) system was patented in 2025 [25]. This technology represents a novel electrical turbo compound layout with supercharging capabilities; its final configuration is shown in Figure 2.

In particular, the novel compressor group (CG) is the missing hardware component that can maintain ICE performance and compensate for the effects of increased backpressure. It is a perfect example of reducing the Backpressure Paradigm's application domain.

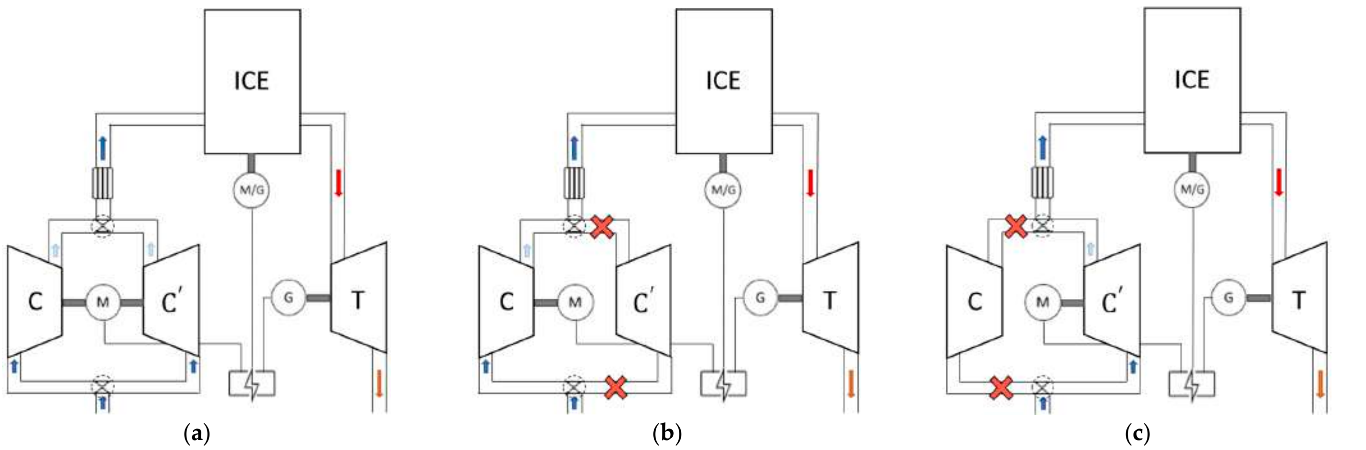

Figure 2. TGEMS schematic: (**a**) Final Layout, (**b**) Working condition 1, (**c**) Working condition 2 [25].

In TGEMS, the CG and the T stages have been decoupled; the CG consists of two distinct-size compressors connected in parallel, with C being the larger and C′ the smaller. The operating logic alternates between two dual working conditions. As shown in Figure 2b, for example, working condition 1 disengages C′, and the two special circular valves divert the flow by closing the passage through C′. This means that, at steady state, each compressor operates alone while the other is disengaged. This configuration allows coverage of a much larger portion of the reduced mass flow rate/pressure ratio plane, as shown in Figure 3. The graph also shows an overlapping region between the C and C′ maps. This is the so-called "crossover region", where switching between C and C′, according to the chosen discriminant condition, can occur.

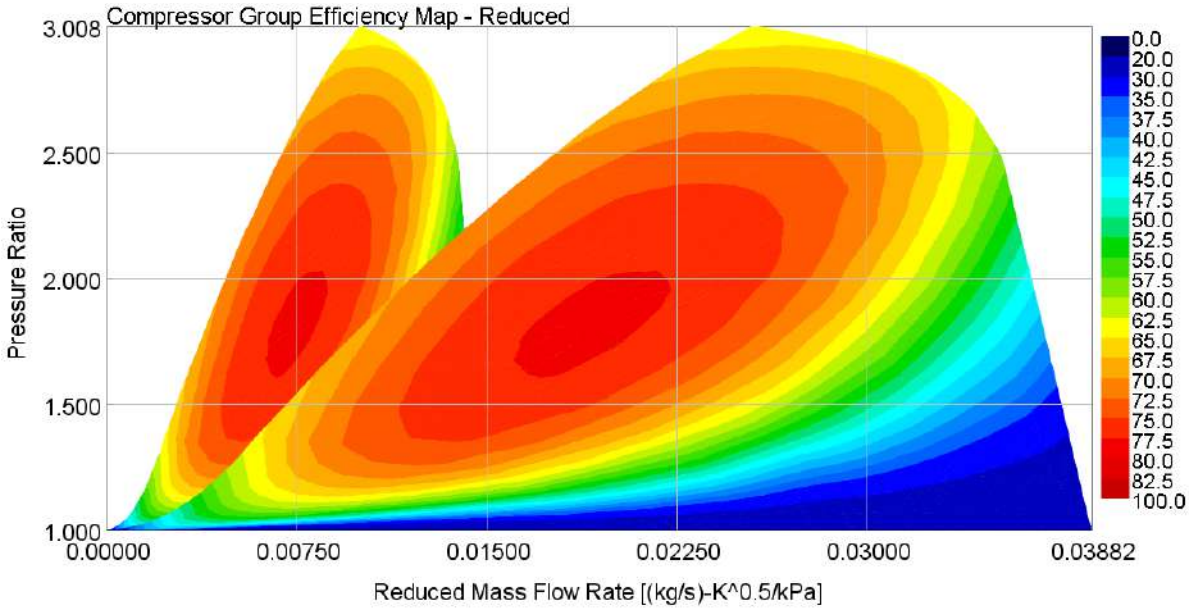

Figure 3. TGEMS Compressor stage: final component Efficiency Map [25].

To maximize the recovery energy and the exhaust backpressure, the wastegate valve was abolished, and the T controller can keep the component always operating in a high-efficiency region, thanks to a math-function-based strategy similar to that proposed by Zhuge et al. [15].

The compressors are PID-based and controlled with the main purpose of reaching a stable steady-state operation, without considering the fast transient operation as a goal in this research. However, it is important to note that one of the main benefits of TGEMS, from

https://doi.org/10.3390/en19092181

the end user's point of view, is the fast response of the stages, with consequently strong turbo lag reduction.

This paper will demonstrate that the counterintuitive T-stage scaling down leads to a general efficiency increase, a contextual rise in PU total power output, and the possibility of freely controlling the ICE operating line. Indeed, by performing a power balance between the turbo machines and the ICE, the conclusions are not obvious and provide evidence of a so-called "backpressure supercompensation effect" associated with rising exhaust backpressure, whose influence and operational limits will be studied and discussed.

To achieve this purpose, the research followed a stepwise procedure in which the TGMES was first applied to the baseline without scaling down the T stage, creating references for the two main energy management strategies. After this step, the T stage was progressively scaled down while maintaining coherence with the chosen energy management strategy. Finally, the influence of the chosen energy management strategy was assessed to explore the possibility of controlling the ICE operating line.

In particular, a 100% load benefit of roughly 5% *bsfc* reduction at 5000 rpm, with a contextual maximum power output increase of around 9%, was also achieved without reducing the T stage. With T scaled to 0.7, peaks of *bsfc* reductions of up to −6.43% at 5000 rpm and 25% load were achieved. With the added possibility to control the ICE operating line, *bsfc* reductions of −7.93% at 5000 rpm and −6.83% at 3000 rpm were also reached.

Based on the results, the TGEMS architecture appears to be a strong candidate for an even more downsized engine, and it paves the way for a new generation of supercharged engine, a "super-backpressured engine", a reference to mild and full hybrid vehicles.

2. Materials and Methods

At this stage of research, given the novelty of the technology and the planned R&D program on the patent [25], the chosen approach aims to confirm the main physical phenomena to justify further insights and investments. To this end, only a digital approach was used, and all simulation procedures in this paper have been performed on the GT-Suite (v2016) platform, including the model creation and the TGEMS design.

2.1. Baseline Engine and Turbulent Combustion Model Creation

Without access to a real ICE, a detailed and realistic baseline code is needed to ensure high reliability, repeatability, and robust prediction of the results. Therefore, in this phase, the analysis was conducted using a 1-D simulation code (Figure 4) for a well-designed engine already available in GT-Power. A 2.0 L 4-cylinder 4-stroke turbocharged gasoline direct injection (GDI) engine with a wastegate controller and a semi-predictive intercooler was chosen as the baseline engine.

This choice ensures that the order of magnitude of the results, as well as the physical phenomena and related trends, will be maintained as future experimental data become available.

Based on the mean features of the baseline engine, reported in Table 1, the nearly unitary ratio between S and B indicates that this engine is suitable for a passenger car. Its performance in terms of P_b and M_b also makes it suitable for segment C-D or SUV hybrid vehicles.

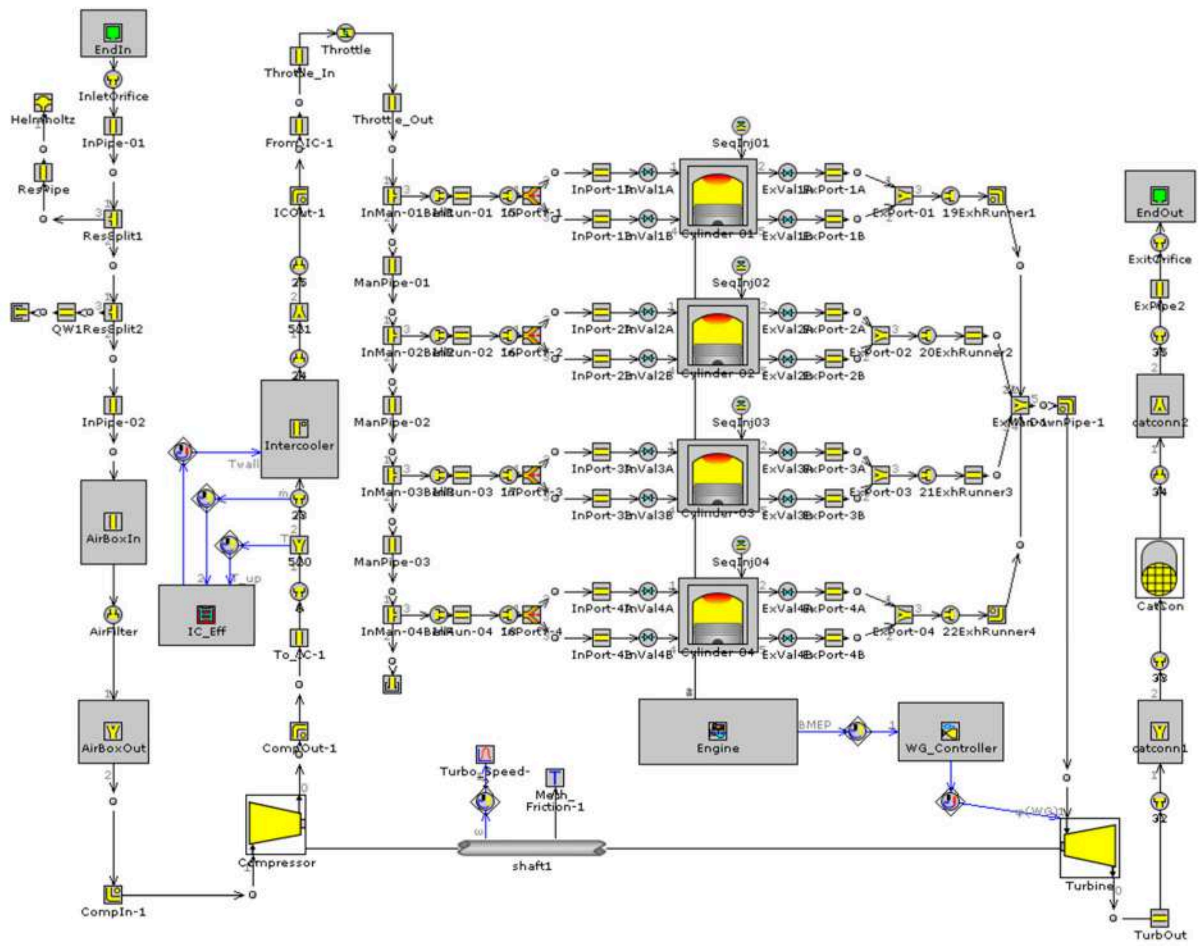

Figure 4. Baseline Engine 1-D model on GT-Suite platform.

Table 1. Baseline engine main features.

N. cylinders	-	4
Unitary displacement	V_d	0.500 cm^3
Total displacement	$V_{d,tot}$	2000 cm^3
Bore	B	86 mm
Stroke	S	86.07 mm
Connecting rod length	l	175 mm
Volumetric compression ratio	r_c	9.5
Type of injection	-	Direct
Max brake power (5000 rpm)	$P_{b,max}$	156.26 kW
Max brake torque (3000 rpm)	$M_{b,max}$	297.57 Nm
Max brake mean effective pressure	$bmep$	18.75 bar

The baseline main reference was defined using 5 simulation cases already set within the program, without any modifications:

- 5 runs with steady state goal,
- Wide opening throttle (WOT),
- 5 representative rotational speed conditions.

The main characteristic curves in terms of P_b, M_b and $bsfc$ are shown in Figure 5.

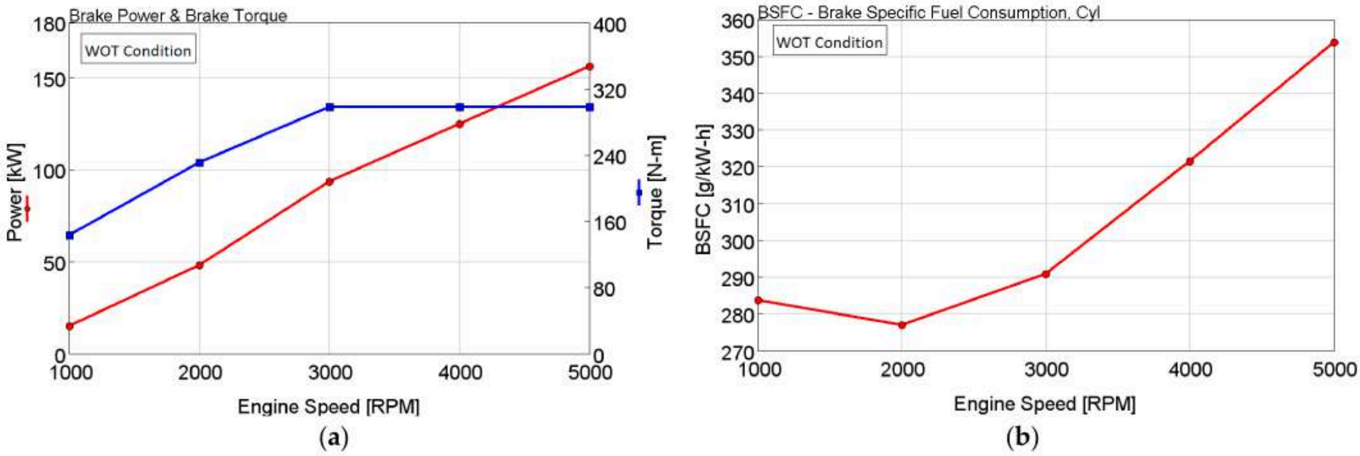

Figure 5. Baseline main characteristic curves in WOT: (**a**) P_b and T_b, (**b**) *bsfc*.

The engine reference model is based on a Wiebe function to describe combustion [26,27]. This combustion model has already been calibrated by the baseline maker across the main operating range. From the literature, the Wiebe function allows the mass fraction burned x_b to be evaluated empirically.

$$x_b = \left\{ 1 - e^{\left[-a \left(\frac{\theta - \theta_0}{\Delta\theta} \right)^{m+1} \right]} \right\} \tag{1}$$

where a is the efficiency parameter, θ is the crank angle in degrees, θ_0 is the start of combustion crank angle in degrees, $\Delta\theta$ is the burn duration, and m is the Wiebe shape function [26,27].

In the baseline, using (1) the combustion process is modeled, and the heat transfer within the cylinder is evaluated using the Woschni model. In this case, since x_b is not related to a physical phenomenon, the baseline model does not consider important parameters like [20] (pp. 368–427) [28]:

- turbulence intensity,
- Kolmogorov scale,
- turbulent flame speed,
- flame–cylinder wall interactions.

Given the role of the compressor group in maintaining the ICE baseline performance in a TGEMS-equipped engine, the knock phenomenon must be carefully considered to avoid unfeasible operating conditions in a spark ignition (SI) engine [29–31].

To account for knock, the Wiebe model was replaced with a turbulent combustion model, the SI-Turb [32]. Unlike Wiebe, the SI-Turb model is based on the physical relationship between fuel and laminar and turbulent flame speeds, making it predictive and more suitable for knock-limited conditions [20] (pp. 368–427).

Unlike Wiebe, implementing SI-Turb as a combustion model requires defining:

- a flow object that specifies flow characteristics in the cylinder,
- a flame geometry object that describes the geometry of the head and piston and the location of the spark.

These were extracted from another mono-cylinder 1-D model with the same geometric features as the baseline engine, already available in the program.

To proceed with the simulations, the new combustion model needed to be calibrated to reproduce the Wiebe-based data:

- 50% BurnPoint was set as the combustion anchoring option, and the same Wiebe anchor angles were applied to each simulation case to maintain the same combustion barycenter,

- Gasoline was selected as fuel for laminar speed evaluation,
- Flame Kernel Growth and Taylor Length Scale Multipliers were tuned [32] to match the pressure trend obtained from Wiebe.

As shown in Figure 6, the SI-Turb in-cylinder pressure trends fit the Wiebe model almost perfectly, except for the 1000 rpm case, where differences are evident in the post-ignition rise and in the peak pressure (increased by about 10%).

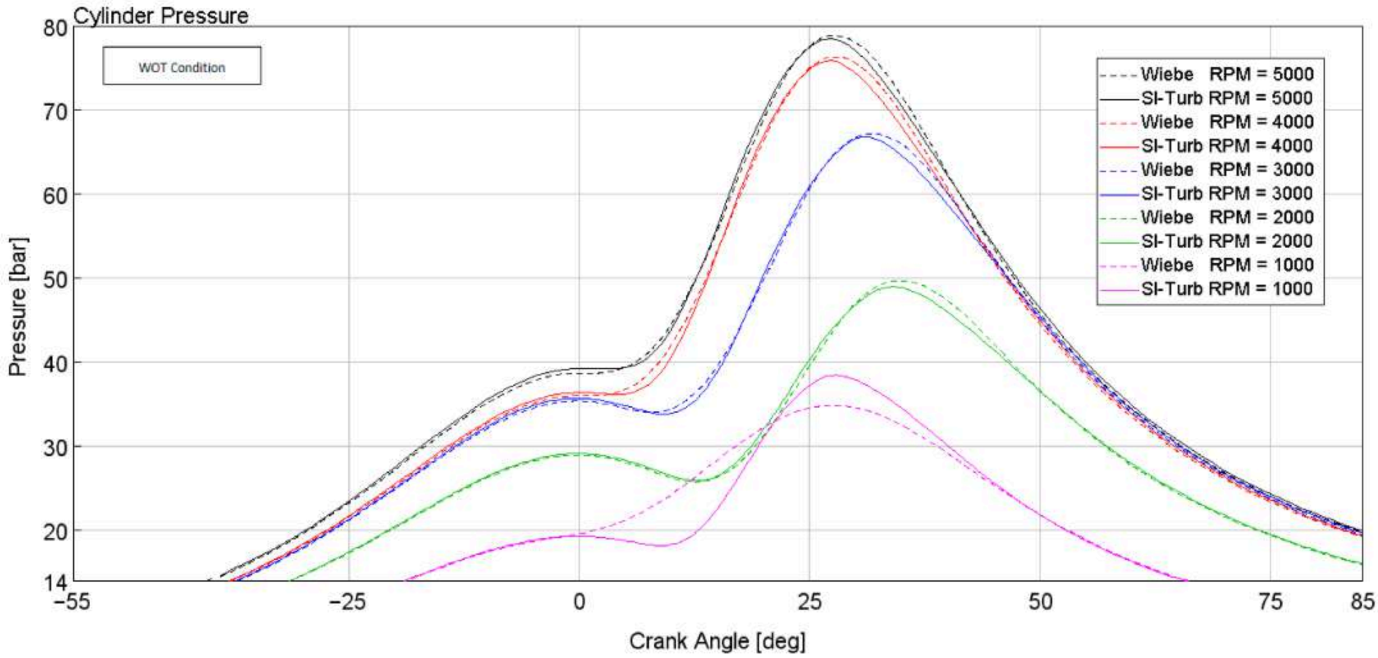

Figure 6. Calibration of SI-Turb model: Cylinder pressure trend for each simulation case.

This behavior can be explained by examining the *m* value in Wiebe. In the program, the parameter m appears to be constant and equal to 2 (a typical value [20] (pp. 368–427)). However, the literature shows that *m* depends significantly on engine speed and brake mean effective pressure (*bmep*) [26,33,34]. This suggests that it was probably originally calibrated for medium–high loads to make it suitable for all simulation points. Given the planned partial-load simulations, the transition to SI-Turb is even more justified.

Furthermore, the new trend at 1000 rpm appears more credible because Wiebe seems to underestimate the combustion speed in this case. As evident from Table 2, at 1000 rpm in Wiebe, the corresponding spark advance (SA) associated with the 50% burned crank angle (CA50) appears overly advanced; each angle is expressed at top dead center firing (aTDCf).

Table 2. SA related to CA50 comparison for each rotational speed.

Engine Speed [rpm]	Wiebe Spark Advance [deg aTDCf]	SI-Turb Spark Advance [deg aTDCf]	CA50 [deg aTDCf]
5000	−0.91	−10.22	21.00
4000	−0.91	−7.53	21.00
3000	3.09	−2.59	25.00
2000	7.13	1.61	28.00
1000	−6.17	1.69	22.00

In Figure 7, the calibration of the SI-Turb combustion model can be assessed by comparing the main in-cylinder temperatures and the *bsfc* trends. Except for the 1000 rpm case, for the same reasons mentioned previously, all trends are superimposed on the Wiebe curve or translated by negligible amounts.

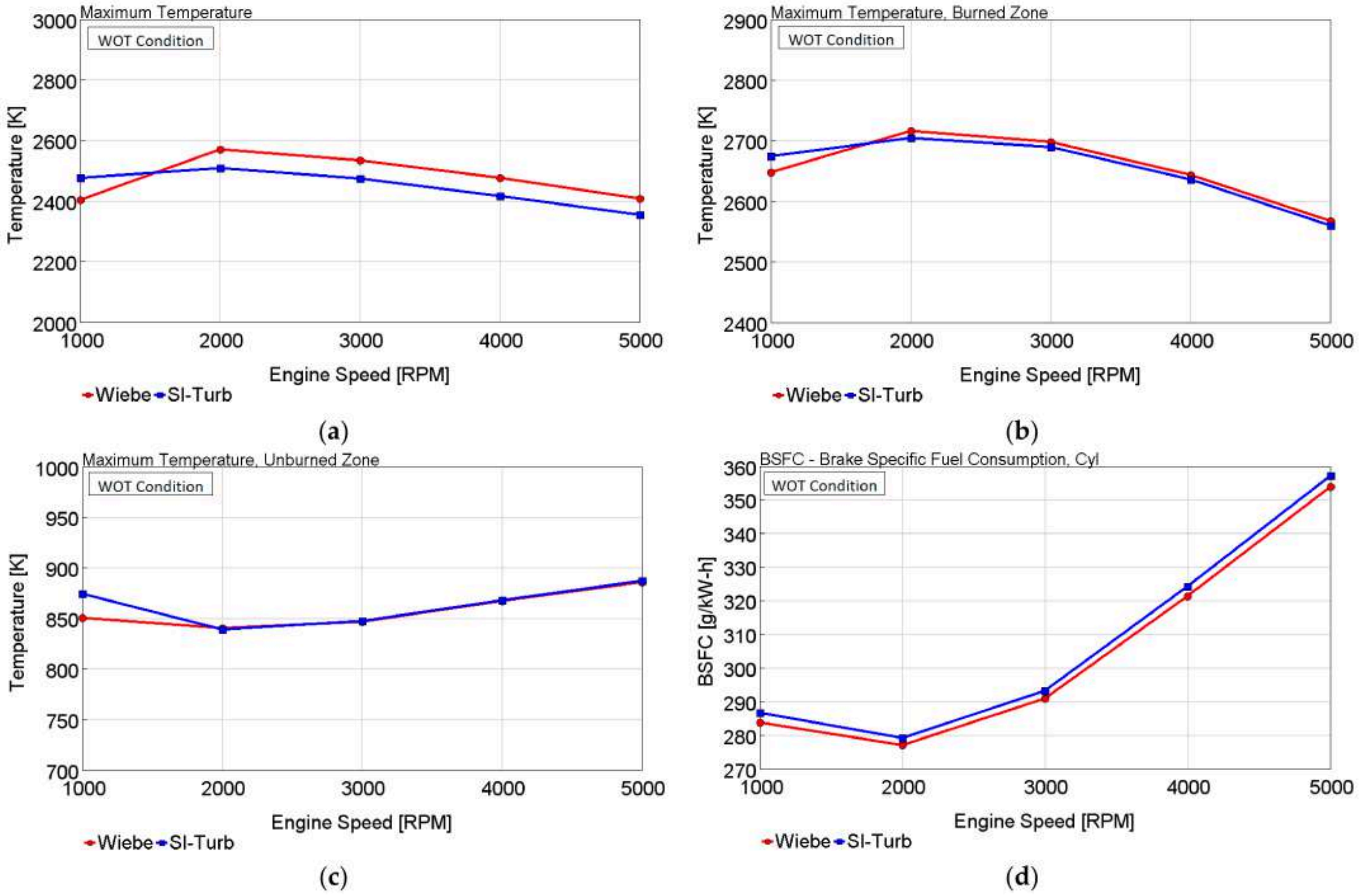

Figure 7. Calibration of SI-Turb model: (**a**) maximum temperature, (**b**) maximum burned zone temperature, (**c**) maximum unburned zone temperature, (**d**) *bsfc*.

To conclude the baseline case definition, a predictive Douaud and Eyzat [27,35,36] knock model was selected and calibrated. In particular, the Knock Induction Time Multiplier [32] and the Knock Index Multiplier [36] are knock calibration parameters, and they were tuned to obtain realistic knock induction time integral values.

According to the literature, knock occurs when the induction time integral equals 1 [27,32,36,37]:

$$\int_{time=0}^{time_{knock}} \frac{1}{\tau} dt = 1 \tag{2}$$

In which τ is the ignition delay.

The resulting integral values in WOT, derived from the knock calibration, are reported in Table 3. The model has been set to obtain safe values that are not far from the knock condition; in this way, an overestimation of the integral value would indicate a higher safety margin.

Table 3. Calibration of SI-Turb model: Knock induction time integral values.

Engine Speed [rpm]	Knock Induction Time Integral [-]
5000	0.511
4000	0.530
3000	0.551
2000	0.504
1000	0.603

2.2. TGEMS 1-D Modeling and Set-Up

Starting from the original 1-D model in Figure 4, the TGEMS was implemented by replacing the shaft connection inside the turbocharger with two shafts of the same specification. To simplify the system, rotations were imposed using 1-D rotational mechanical components. Furthermore, the wastegate valve and its controller were removed. The resulting complete TGEMS model is shown below in Figure 8.

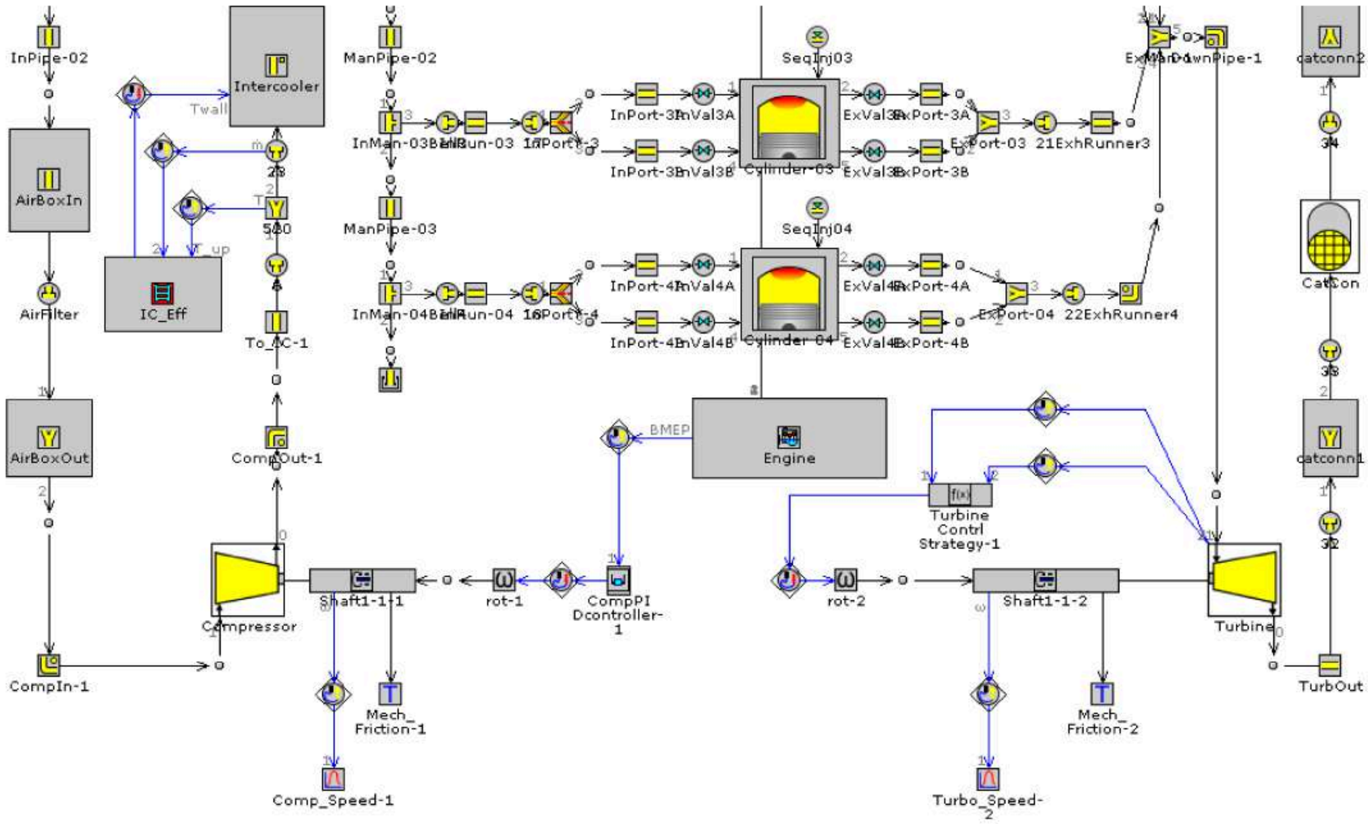

Figure 8. TGEMS Engine: 1-D model detail on GT-Suite platform.

To control the turbomachines, a *bmep*-target PID controller was set and connected to a compressor component that represents the group C-C′, while a controller based on a mathematical equation was set and connected to a turbine component that represents T to apply the control strategy.

The main turbomachine quantities are defined as:

$$N_{red,t} = \frac{n_t}{\sqrt{Temp_{in,t}}}\ ,\ \ \beta_t = \frac{p_{in,t}}{p_{out,t}}\ ,\ \ \dot{m}_{red,t} = \dot{m}_t \frac{\sqrt{Temp_{in,t}}}{p_{in,t}} \tag{3}$$

$$N_{red,c} = \frac{n_c}{\sqrt{Temp_{in,c}}}, \beta_c = \frac{p_{out,c}}{p_{in,c}}, \dot{m}_{red,c} = \dot{m}_c \frac{\sqrt{Temp_{in,c}}}{p_{in,c}} \tag{4}$$

The T control strategy is based on the use of pressure ratio β_t and inlet temperature $Temp_{in,t}$ as input parameters for the function (5) to evaluate the turbine rotational speed n_t needed to reach the maximum possible efficiency; in particular, a polynomial approximation was iteratively determined to express the reduced speed $N_{red,t}$ as a function of β_t and turbine efficiency η_t as shown in Figure 9. In this way n_t becomes a function of:

$$n_t = f\left(\beta_t\ ,\ Temp_{in,t}\ ,\eta_t\right) \tag{5}$$

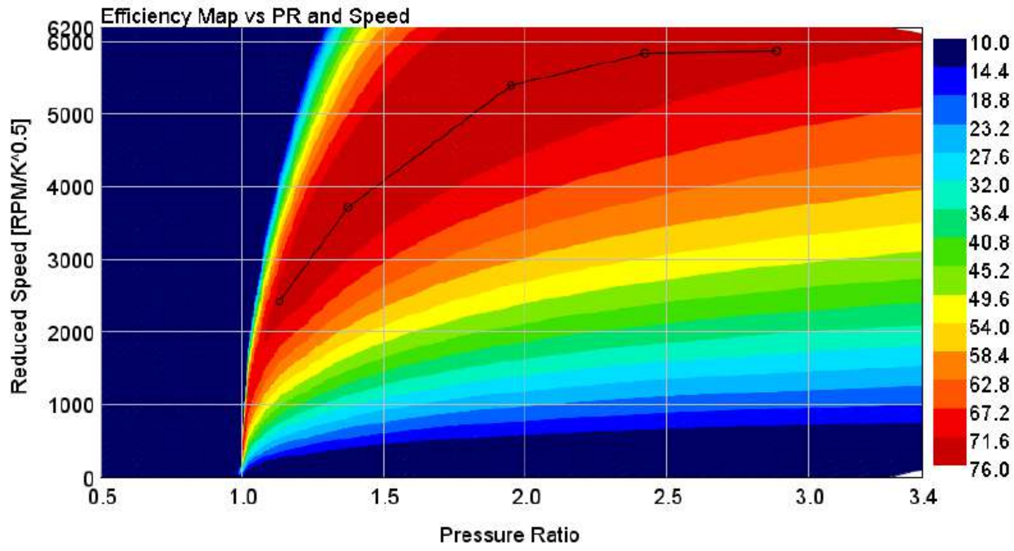

Figure 9. T Efficiency map after optimization.

Thus, the function (5) defines a suitable strategy for various loading conditions.

The logic is to control n_t by adjusting the excitation parameters of the generator [6,15]. It is highlighted that, unlike other application examples in the literature, such as those by Zhuge et al. [15] and Zi et al. [6], the same purpose was achieved using only p and $Temp$ data, without a mass flow rate sensor.

The operation of the C or C′ compressor was achieved using a variable mass multiplier parameter. Starting from the default value of 1, the compressor can be scaled up or down by increasing or decreasing the parameter, respectively. To ensure sufficient coverage of the plane $\left(\dot{m}_{red,c},\ \beta_c\right)$, the mass multiplier was set to 1.2 for C and 0.47 for C′.

Following the same approach, the T power output and the backpressure were progressively increased by reducing the turbine mass multiplier factor from 1 to 0.7.

Following a similar approach to Zi et al. [6], in the absence of electric machines, their presence was simulated by imposing constant efficiency terms for the electric motor and generator. In this way the total TGEMS PU brake power $P_{b,tot}$ can be expressed as:

$$P_{b,tot} = P_b + P_t \cdot \eta_{el,g} + \frac{P_c}{\eta_{el,m}} \tag{6}$$

Usually, $\eta_{el,g}$ is not equal to $\eta_{el,m}$ because the transfer battery efficiency must also be considered during the recharging process [6]. However, by allowing the power flow to satisfy the driving mission directly, without passing through the battery, and noting the small difference between the two terms during recharging, they can be equated. Thus, the equation becomes:

$$P_{b,tot} = P_b + P_t \cdot \eta_{el} + \frac{P_c}{\eta_{el}} \quad \Rightarrow \quad P_{b,tot} = P_b + P_{el} \tag{7}$$

With η_{el} set equal to 0.9.

Equation (7) means that in a TGEMS the *bsfc* evaluation needs to be computed by considering not only P_b but $P_{b,tot}$, so:

$$bsfc = \frac{\dot{m}_f}{P_{b,tot}} \quad (8)$$

In which $\dot{m}_f$ represents the fuel mass flow rate.

3. Results

Even if implementing control logic and analyzing transient engine response and performance over real driving cycles would provide further information and confirmation of benefits, from a time and cost perspective this approach often turns out to be too demanding [38]. For this reason, a solution was found by selecting a set of representative steady-state working conditions. This approach has been considered a necessary step at this stage of research, and it is consistent with both the main purposes of the article and the method used by Baratta and Misul [38] in a previous research project.

Therefore, to achieve the results, all numerical experiments were conducted by simulating and comparing four different loading conditions at five representative engine rotational speeds:

- Loads: 100% to 25% (of baseline *bmep*),
- Engine speed: 5000 to 1000 rpm,
- Simulations end when the steady-state condition is reached.

The workflow begins with demonstrating the effectiveness of the TGEMS in its basic implementation, followed by the "backpressure supercompensation effect" analysis.

In this context, the absence of the electrical subsystem, including the battery, converters, and state-of-charge dynamics, and the use of (7) are simplifications that do not compromise the analysis.

3.1. TGEMS Benefits Without T Scaling Down and Technology Potential

The comparison between the baseline and TGEMS was performed considering a baseline case with *bsfc* optimized. In this condition, the wastegate opening and the CA50 at partial loads were tuned to minimize the *bsfc* value for each simulation case. To avoid the influence of other phenomena, once determined, the CA50 was not changed in TGEMS relative to the baseline simulation. The results of this optimization are shown in Table 4.

Table 4. Baseline case *bsfc* optimized: CA50 values for each simulation case.

	Load 100%	**Load 75%**	**Load 50%**	**Load 25%**
Engine Speed [rpm]	**CA50 [deg aTDCf]**	**CA50 [deg aTDCf]**	**CA50 [deg aTDCf]**	**CA50 [deg aTDCf]**
5000	21.00	14.00	8.00	6.00
4000	21.00	14.00	8.00	6.00
3000	25.00	18.00	12.00	10.00
2000	28.00	21.00	15.00	13.00
1000	22.00	15.00	9.00	7.00

Being designed for a hybrid vehicle solution, the TGEMS system can meet the target load and satisfy the mission by following two power management strategies:

- Pure thermal,
- Power-split.

In pure thermal mode, the drive mission is satisfied by the ICE alone, and the excess electrical power produced is stored in the battery. Instead, during full power-split mode, $P_{b,tot}$ is equal to the P_b produced by the baseline ICE, and no energy flows through the battery.

In Figure 10, the two resultant *bsfc* maps were compared. In the TGEMS map, the two power management strategies were simulated. It appears evident that the best strategy depends on the relative position of the considered load curve with respect to the optimum operating line (OOL). By observing the map, in accordance with the literature [20] (pp. 32–36):, the OOL seems to be near the 75% load line. Therefore, if the curve is above 75% load, the power-split will be more effective, because it shifts the ICE load curve downward, bringing it closer to the OOL. Conversely, if the curve is below 75% load, the pure thermal will be more effective, because it shifts the ICE load curve upward. This is the reason the 25% power-split curve was not simulated.

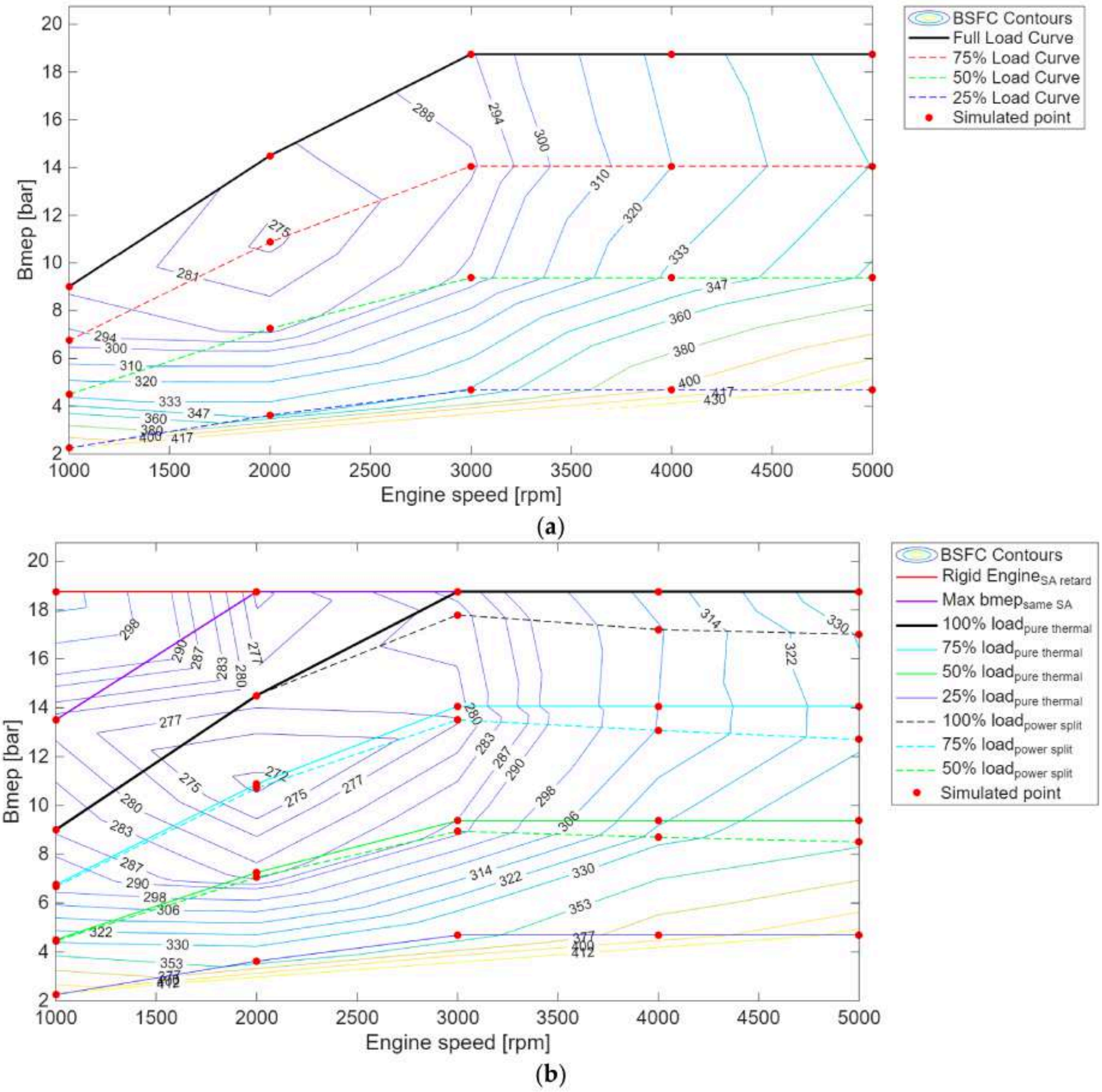

Figure 10. *bsfc* map and partial load curves comparison: (**a**) Baseline, (**b**) TGEMS.

It is evident that the TGEMS application, even without T scaling down (mass multiplier equal to 1), makes it possible to achieve a significant decrease in *bsfc*, with a corresponding extension of the achievable *bmep* at low engine rotational speed.

On the TGEMS map, the purple curve represents the maximum achievable *bmep* without retarding combustion relative to the baseline. Instead, by retarding combustion at 1000 rpm, the red line was achieved; by paying a *bsfc* penalty, it defines a rigid engine characteristic in which the torque remains constant.

Regarding the feasibility of the simulated point, the trend in knock tendency under the worst-case scenarios is shown in Figure 11.

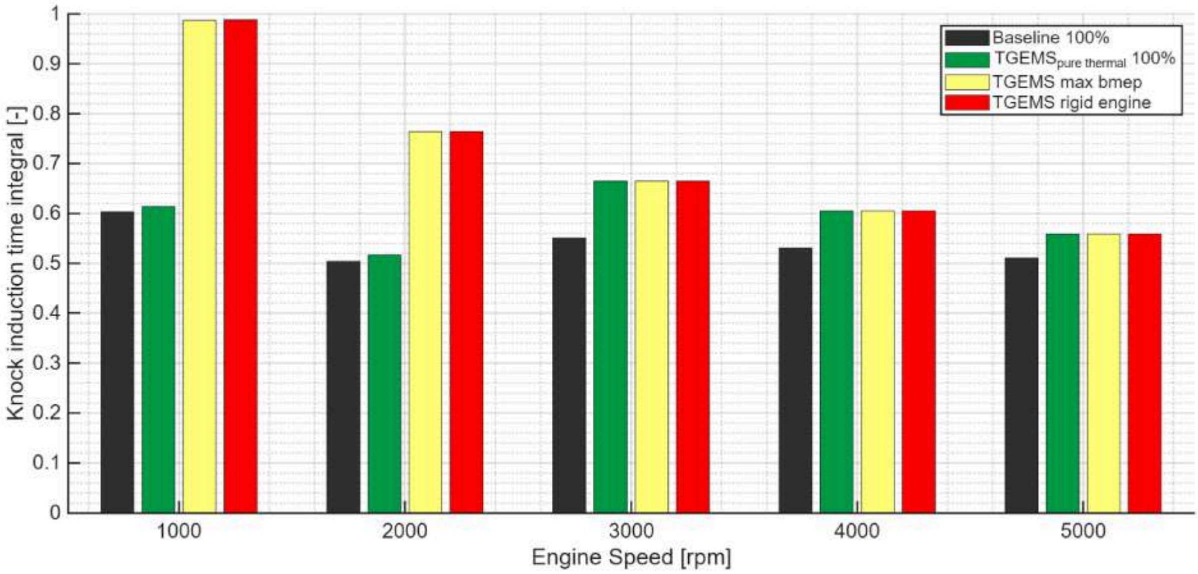

Figure 11. Knock induction time integral comparison in the most critical load conditions.

As was reasonable to expect, as shown in Figure 10, the TGEMS working points with a *bmep* higher than the baseline maximum represent the most critical scenarios, because a combination of higher boost pressure, higher exhaust backpressure, and higher achieved *bmep* occurs. In particular, to reduce the integral value and obtain the red bar at 1000 rpm, the CA50 was moved from 22 to 36 deg aTDCf to retard the spark advance.

To provide a numerical measure of the maximum performance benefits and the potential for ICE technology downsizing, Table 5 was assembled. The comparison was made with respect to the baseline case under full-load conditions to show the main numerical values indicated in Figure 10.

Table 5. Main quantities comparison: full-loaded Baseline vs. TGEMS at maximum simulated loading conditions.

	Baseline (100% Load)			TGEMS (Max *bmep*)				
Engine Speed [rpm]	**P_b [kW]**	**M_b [Nm]**	***bsfc* [g/kWh]**	**$P_{b,tot}$ [kW]**	**M_b [Nm]**	***bsfc* [g/kWh]**		**Δ*bsfc* [%]**
5000	156.3	298.6	357.1	170.0	298.4	339.5		−4.92%
4000	125.0	298.5	324.2	135.4	298.2	309.4		−4.55%
3000	93.78	298.5	293.3	98.48	298.4	284.2	⇒	−3.11%
2000	48.35	230.9	279.2	62.39	298.2	274.4		−1.70%
1000	15.00	143.3	286.7	22.03	214.8	278.5		−2.88%
				TGEMS (rigid engine)				
1000	15.00	143.3	286.7	29.76	298.4	311.1		+8.49%

Thanks to the higher compressor unit capability, the total PU power and the ICE torque increase significantly at 2000 and 1000 rpm. Without retarding combustion, a power output variation of +29.02% at 2000 rpm and +46.83% at 1000 rpm was achieved, with a torque increment of +29.18% at 2000 rpm and +49.96% at 1000 rpm. Instead, for the rigid engine simulation, the only difference from the previous case occurs at 1000 rpm, with +98.37% power and +108.30% torque.

In the base configuration, the TGEMS system increased the maximum power output by +8.75% at 5000 rpm, with a contextual −4.92% in *bsfc*, and made it possible to satisfy drive missions not covered by the baseline engine.

3.2. T-Stage Scaling Down and the Backpressure Supercompensation Effect

The previous results and Figure 10 indicate that, despite the increase in exhaust backpressure due to the wastegate abolition, the *bsfc* decreases significantly in almost all simulation cases. To analyze this apparently counterintuitive behavior, the phenomenon was isolated by comparing the baseline and the TGEMS in the same ICE operating condition. In this way, the influence of other physical phenomena has been limited.

In particular, the *bmep* conditions not reachable from the baseline engine were no longer considered, nor was the power-split loading curve, to maintain a constant distance from the OOL. However, the magnitude of the power-split influence in reducing *bsfc* will be shown at the end of this subsection.

To achieve higher exhaust backpressure, the T stage was progressively scaled down by reducing the corresponding mass multiplier, and the simulations in the four main loading conditions were repeated.

Four different mass multipliers were tested: 1, 0.9, 0.8, and 0.7, with 1 as the baseline. They define four different T: T1, T0.9, T0.8, and T0.7, each scaled down by an additional 10% relative to the baseline T1.

The simulation results are shown in Figure 12 and provide evidence of two effects:

- $P_{b,tot}$ monotonously increasing trend,
- *bsfc* reduction trend dependency on T dimension and load–engine speed window.

If the first phenomenon has been predicted due to the higher enthalpic drop in the T stage when T scaling down occurs, together with the second, it indicates the presence of a “backpressure supercompensation effect”. This means that, within a certain window, the higher P_c needed to reach the *bmep*, as well as the higher pumping work, are supercompensated by the higher P_t produced in the T stage. This allows peaks of *bsfc* reductions of up to −6.43% with T0.7 at 5000 rpm and 25% load.

It is important to note that, in Figure 12a, the red columns at 5000 rpm are missing. They have been removed because the compressor group was unable to provide the requested boost pressure to reach the target *bmep*. This represents the first limit of the T-stage scaling-down process.

A clear view of this limitation is shown in Figure 13, where the trends of the compressors’ group working curve at various T-stage dimensions are compared within the component efficiency map. As evident, the red line reaches the end of the map before the *bmep* target is reached. However, the compressor C cannot be indefinitely enlarged without reducing the crossover region between C and C′ too much.

Anyway, the maximum achievable power output increases from +8.75% at 5000 rpm with T1 to +11.04% with T0.8.

Regarding the operative region where the *bsfc* reduction occurs, Figure 12 shows that this window shifts depending on the loading condition. To analyze this phenomenon, different maps can be extracted using the data in the histograms.

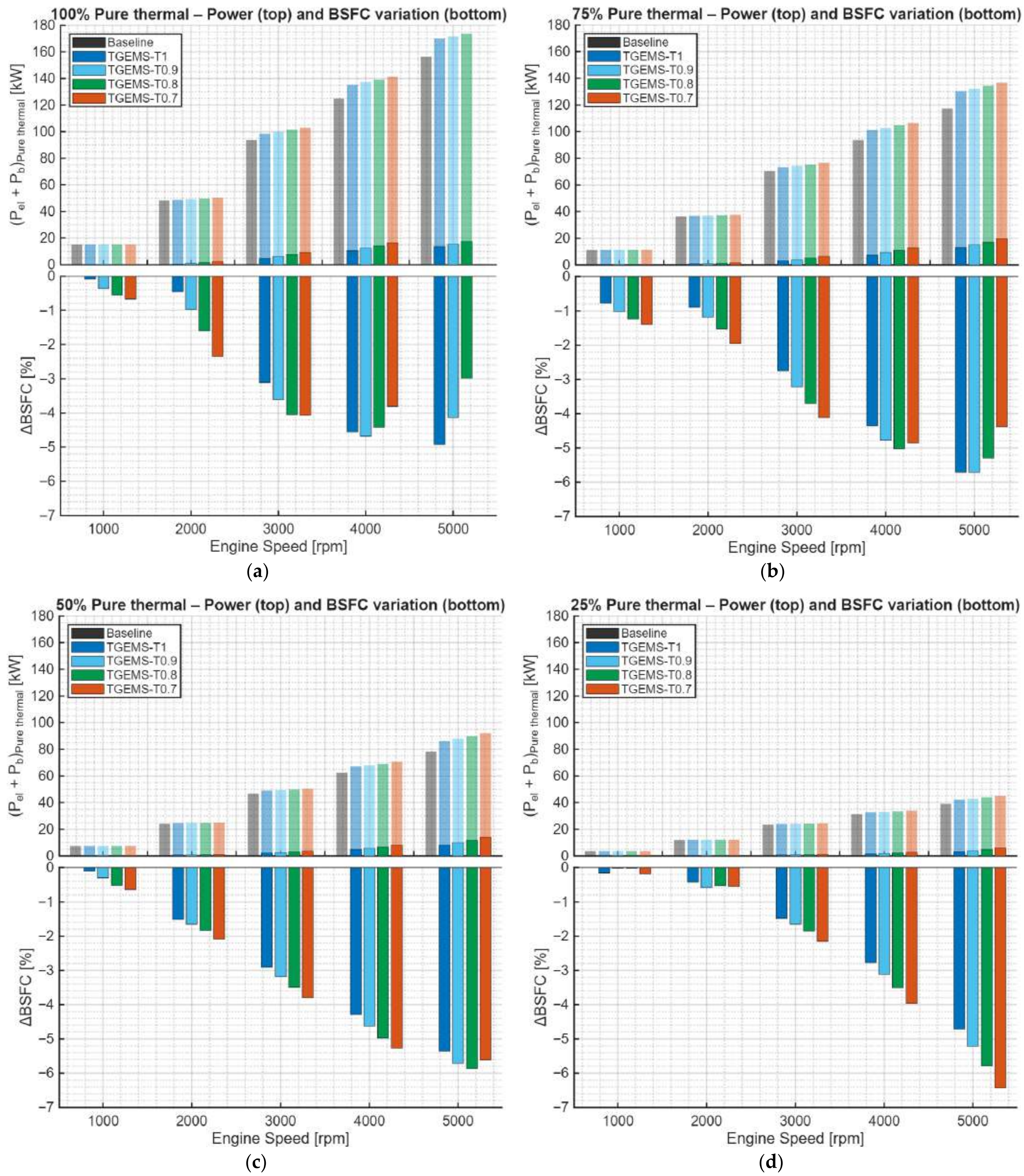

Figure 12. $P_{b,tot}$ and $\Delta bsfc$ variation as a function of T-stage dimension in 4 different pure thermal loading conditions (baseline *bmep*), with $P_{b,tot}$ explicit components (P_{el} solid and P_b transparent): (**a**) 100% load, (**b**) 75% load, (**c**) 50% load, (**d**) 25% load.

Figure 14 presents a comparison of the TGEMS system with the baseline.

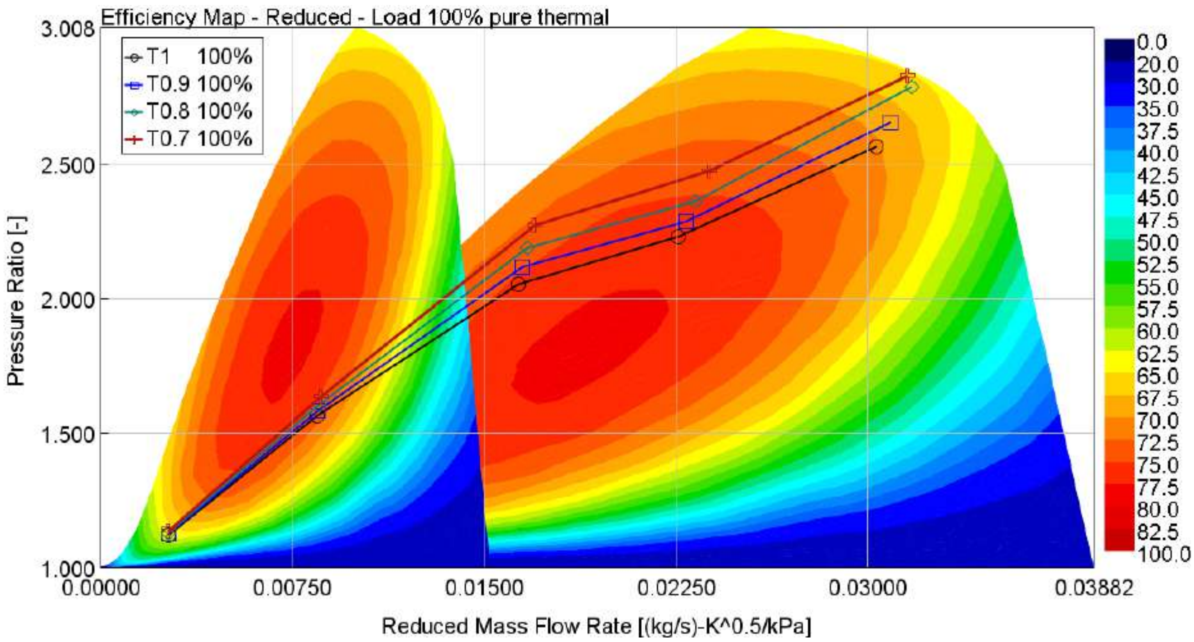

Figure 13. TGEMS compressor stage efficiency map: comparison between working points at 4 different T-stage dimensions in 100% pure thermal loading condition.

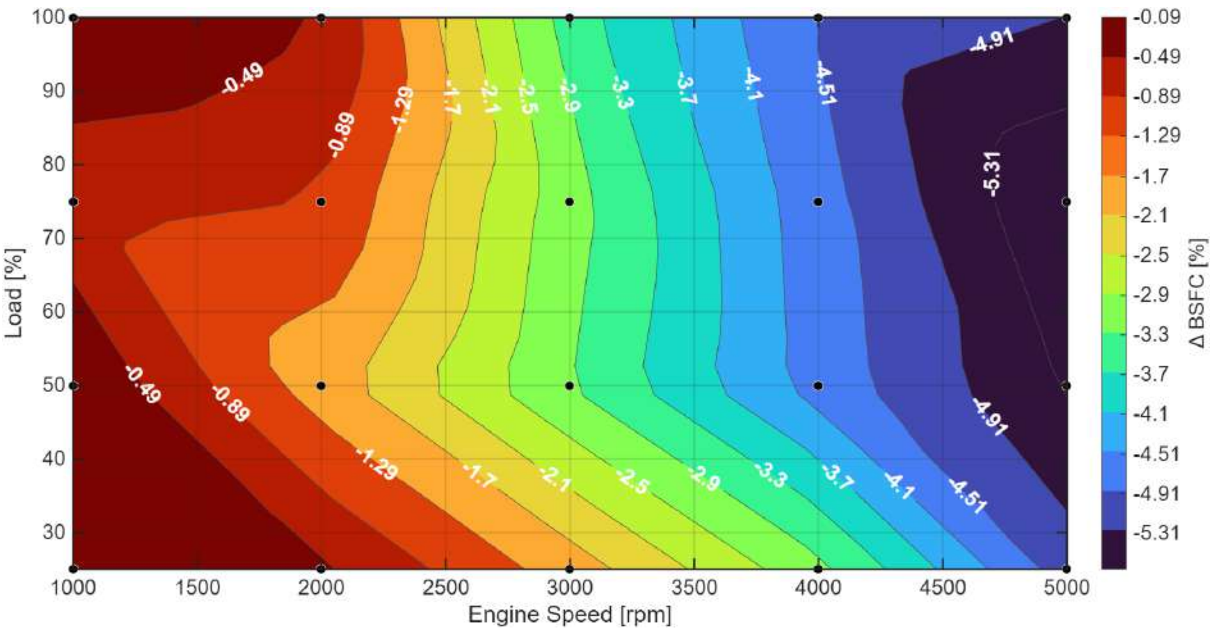

Figure 14. $\Delta bsfc$ map between baseline and TGEMS before T-stage scaling down in pure thermal condition.

It is useful for visualizing the benefits in terms of *bsfc* when the first step of backpressure increase occurs, with the wastegate abolished. It is important to remember that, together with the rising backpressure, the different architecture of the charging groups plays a relevant role in *bsfc* reduction. For this reason, this map (or the TGEMS T1 blue bars in Figure 12) can be used as the reference for isolating the "backpressure supercompensation effect" and for its operative window analysis.

Figure 15 contains maps that make it possible to analyze the backpressure "supercompensation" behavior, because for each T-stage dimension it is possible to observe dependencies on load and rotational speed; the absence of the red columns in Figure 12a is reflected in

Figure 15a because the map is not defined at maximum load and speed conditions when the minimum T dimension is considered.

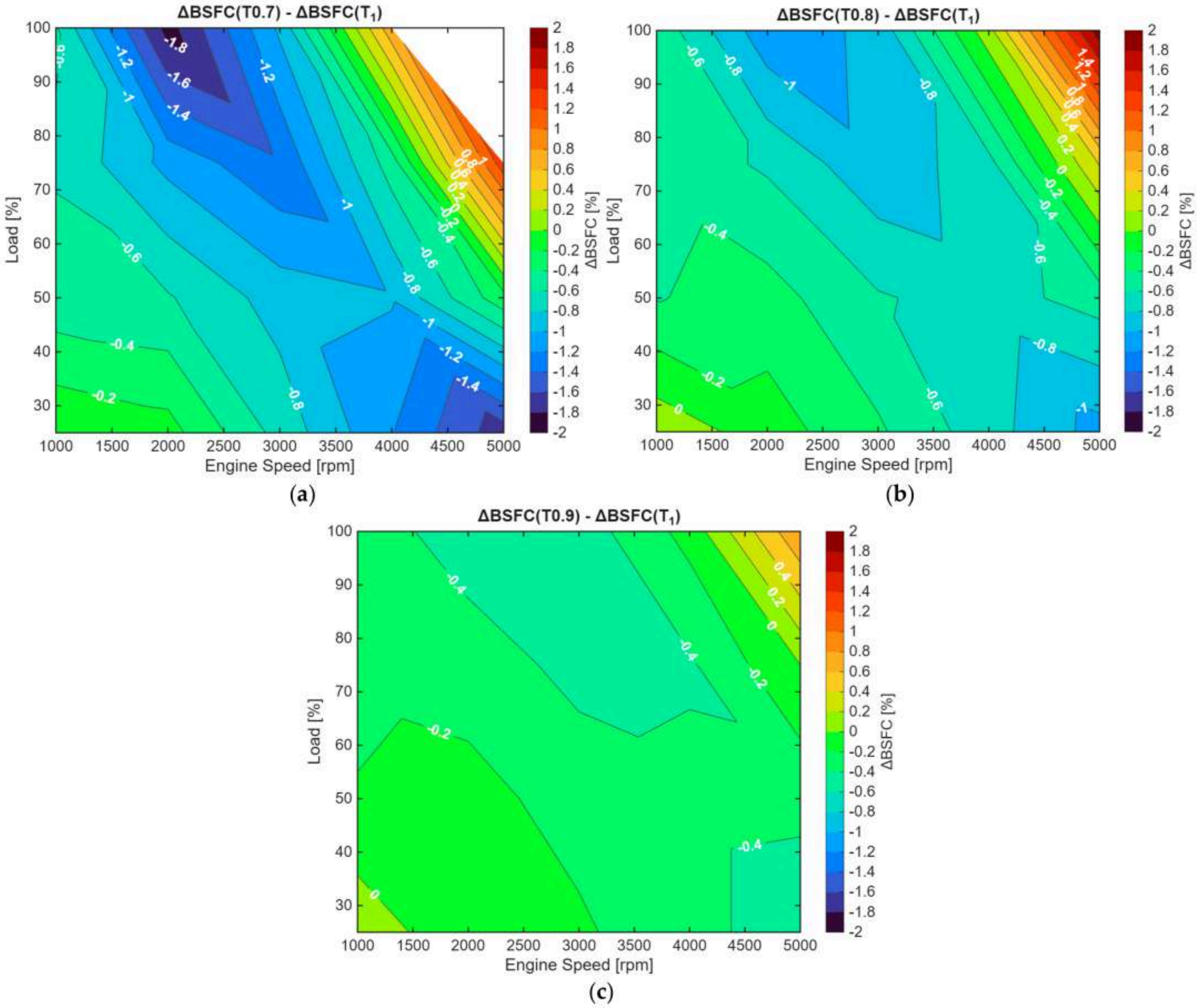

Figure 15. Maps of additional $\Delta bsfc$ due to T-stage scaling-down process, with TGEMS T1 sets as reference—Gains expressed as percentage difference ($\Delta bsfc(Tx) - \Delta bsfc(T1)$): (**a**) $Tx = T0.7$, (**b**) $Tx = T0.8$, (**c**) $Tx = T0.9$.

It appears evident that, once a benefit window is defined at minimum load within a map, it shifts from right to left as the load increases. This means that the maximum gain in *bsfc* translates from the high-speed region at low load to the medium–low-speed region at high load; this defines a large area in which the benefits are maximized.

The comparison of the three maps in Figure 15 also shows that when the T stage scales down, the maximum gain in terms of percentage $\Delta bsfc$ becomes even larger. At the same time, a sliding trend of the $\Delta bsfc = 0$ lane from the upper-right to the lower-left area can be observed during the T scaling process.

The compression of the gain window as backpressure increases represents the second limit of the T-stage scaling-down process.

3.3. Maximum Achieved Benefits and Power-Split Strategy

As seen in Section 3.1, the power-split mode can maximize *bsfc* reduction benefits if the operating line is above the OOL. As shown in Figure 16, if $P_{b,tot}$ remains constant, the T-stage reduction increases P_{el}, but P_b needs to be reduced. This means the engine operating line will move ever closer to the OOL because the process moves ever more fuel-energy exploitation outside the ICE. In this context, the ICE can be seen not only as a device that produces torque but also as a volumetric burner that delivers high-pressure, high-temperature gases to T. This allows new peaks of *bsfc* reduction, such as −7.93% with T0.8 at 5000 rpm and −6.83% with T0.7 at 3000 rpm.

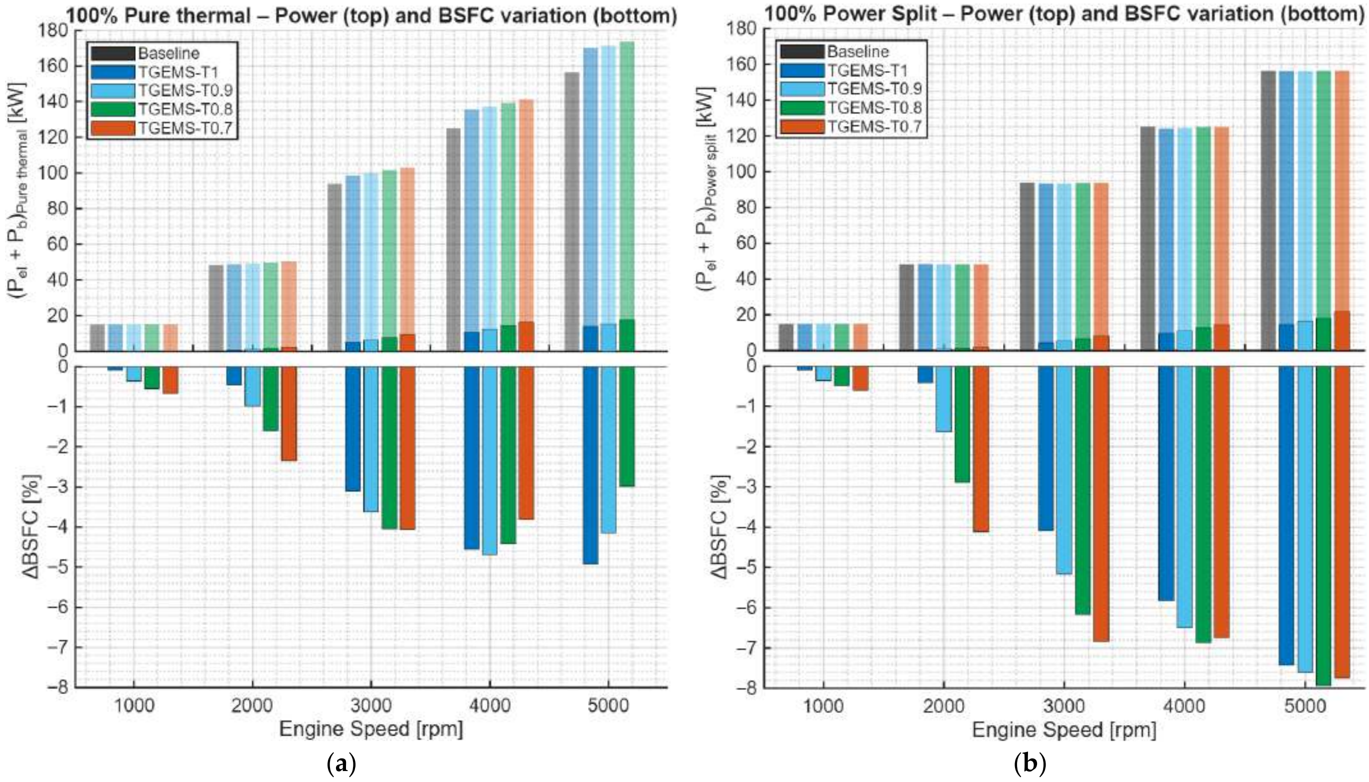

Figure 16. $P_{b,tot}$ and $\Delta bsfc$ variation in function of T-stage dimension in 100% loading condition (baseline $bmep$) with different energy management strategies and $P_{b,tot}$ explicit components (P_{el} solid and P_b transparent): (**a**) 100% Pure Thermal, (**b**) 100% Power-Split.

In Figure 16b, the large gap between the peaks of the $\Delta bsfc$ bars at medium engine speed indicates a probable high distance from the trade-off condition in that area. This means a high improvement margin in case of further T-stage reduction.

This further analysis revealed that increasing backpressure can be used to move the ICE operating line downward freely. It is important to note that this occurs without changes in $P_{b,tot}$, and during fuel energy exploitation, without requiring an external energy source such as the energy stored in the battery.

Therefore, the "backpressure supercompensation effect" can overcompensate for the higher P_c and the higher pumping work, not only with the P_t produced in the T stage but also by moving the ICE operating line closer to the OOL.

3.4. Energy Balancing and Electrical Availability

While the previous subsections assessed the physical effects behind the "backpressure supercompensation effect" with little regard for the electrical energy balance, it is also important to complete the analysis to confirm the feasibility and sustainability of the compressors' boost from an energetic point of view.

From the observations in Figures 12 and 16, it is already evident that a T-stage reduction always implies an increase in P_{el} values, and P_{el} itself is always greater than zero across all considered operating conditions. Recalling (7), this means that, from an energetic point of view, once the steady-state condition is reached, the balance between P_t and P_c net of electric efficiencies is always positive and increases proportionally with T-stage reduction. A clear representation of this phenomenon can be seen in Figure 17.

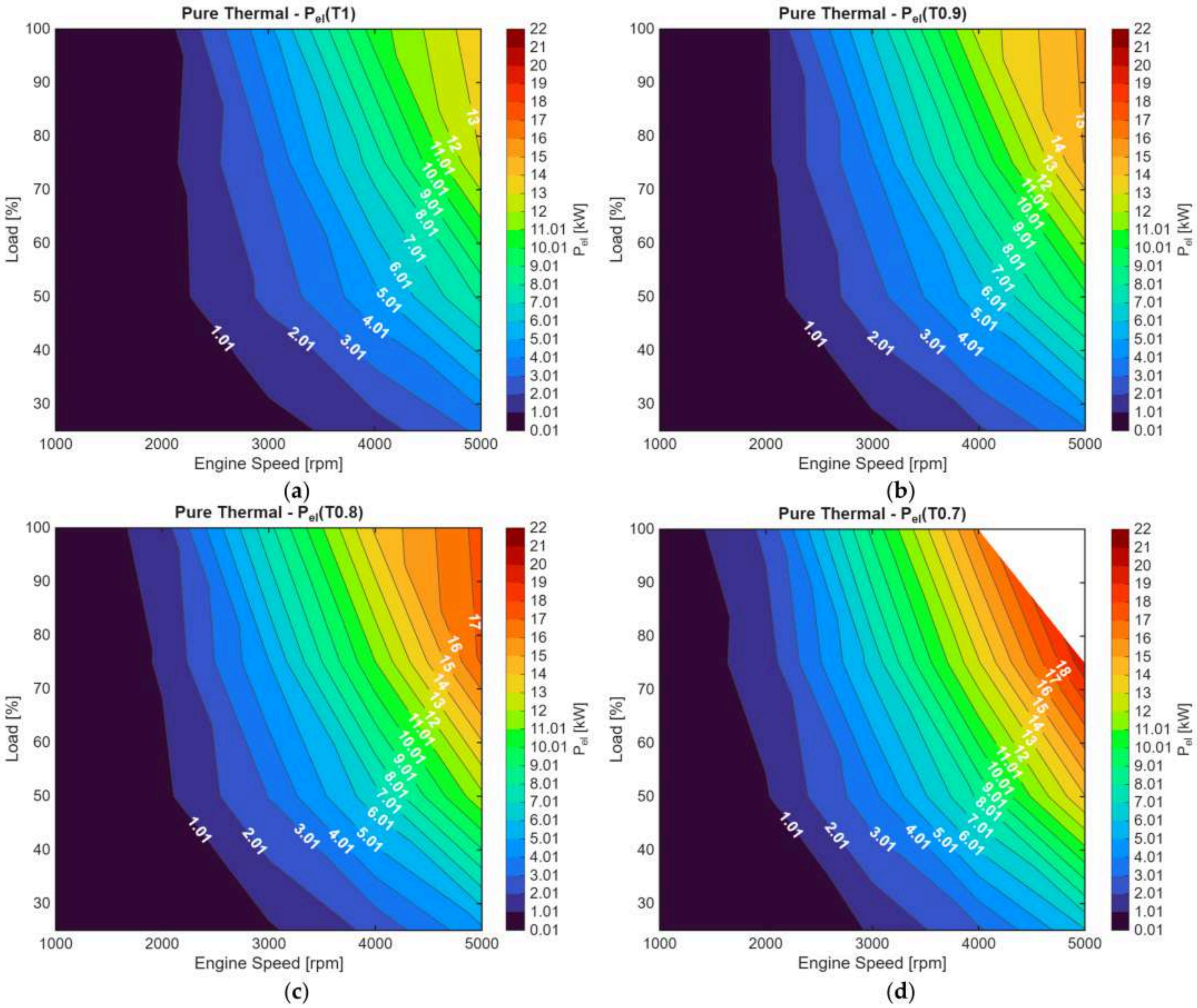

Figure 17. P_{el} distribution maps at different T-stage dimensions, function of load and engine speed in Pure Thermal energy management strategy condition: (**a**) $T1$, (**b**) $T0.9$, (**c**) $T0.8$, (**d**) $T0.7$.

It appears evident that the maximum values in P_{el} are reachable in the high-speed, high-load region. For the same reason mentioned when explaining Figure 12a, the peak P_{el} value is 17.41 kW, obtained at 100% load, 5000 rpm but with T0.8, due to the absence of data for T0.7 under the same conditions. Indeed, the corresponding area in Figure 17d appears blank.

Anyway, the result is consistent with the physics of standard turbines, which require a high expansion ratio to produce power at maximum efficiency. This also explains why, when comparing the four maps, the iso-P_{el} levels shift from right to left as the T stage is scaled down.

This last effect is consistent with what is observed in Figures 12, 15 and 16, and it is particularly interesting because, in a pure thermal strategy, all of P_{el} goes through the battery, and a higher power flow directed to the storage system under medium–low load conditions and medium–low speed means higher charge-sustaining possibilities.

This can be considered an indirect benefit due to the "backpressure supercompensation effect", related to the $P_{b,tot}$ monotonously increasing trend; de facto, the increased exhaust backpressure can not only increase the maximum PU power output but also increase the electrical energy availability.

For completeness, the same trends in Figure 17 also apply to the power-split management strategy; the only difference is that, in this case, the electric power flows directly to the electric powertrain to satisfy the total power request. As expected, the maximum P_{el} peak without the T0.7 limitation is 21.74 kW at 100% load and 5000 rpm, with T0.7.

4. Discussion

The results are extremely promising and confirm all the initial hypotheses. They corroborate that the application domain of the Backpressure Paradigm is not general but strictly related to the ICE boundary conditions. Indeed, with TGEMS, unlike the various examples reported in the literature, the idea of changing the point of view on the main functions of the ICE and considering it like a volumetric burner led to the discovery of various compensation mechanisms never mentioned before. Together, they form the "backpressure supercompensation effect" and make a decrease in *bsfc* achievable, with an increase in PU-specific power high enough to open the doors to new downsizing perspectives and a new generation of "super-backpressured engines".

Indeed, unlike other cited solutions, such as the one by Zi et al. [6], at steady state the TGEMS shows no *bsfc* penalties, with the only exception observed in the "rigid" engine characteristic curve, where combustion was retarded to double the torque and power from the ICE. A similar result can be attributed only to the novel approach used and the supercompensation mechanisms discovered.

The increase in maximum power output at values higher than 10%, achievable from the complete PU, is a key point for further future *bsfc* reduction. It is important to note that the T0.7 at maximum engine speed was not assessed for technical reasons, but a more refined turbo matching study would make it possible to overcome this limit, reaching much higher power targets. Such increases mean the possibility of satisfying the same mission as the baseline engine with units even more downsized. This occurs because the downsizing process moves up the ICE operating points located under the original OOL, bringing them ever closer to the downsized unit OOL, in regions at higher bmep [39]. In a real driving cycle, in which a unit is rarely used at its maximum power rate, this would mean operating at a generally much higher efficiency level.

Furthermore, in hybrid vehicles, the possibility of continuously and perpetually controlling the ICE operating line, without the need for other energy sources at high load, is particularly relevant. Usually, when the ICE operating line is above the OOL, a solution to bring the line closer to the OOL is to reduce the ICE load, compensating for the difference in power output with the electric motor by draining the battery charge [40]. By definition, this strategy is strongly limited by the battery state of charge (SOC) and can be adopted for only a limited amount of time. This explains why hybrid vehicles may be less effective at reducing *bsfc* during steady-state highway use. Instead, it has been demonstrated that a solution like the one discussed in this research and displayed in Figure 16b is self-powered and does not require battery draining or external power sources to operate continuously, making it perfect for long steady-state highway use without any charge-depleting issues.

The same concept is valid, and the system is self-powered even if the purpose is to maximize the power output, directing all the produced power to the wheels, thanks to the positive balancing seen in Figure 17. These possibilities could eliminate or strongly reduce the current compromise between state of charge (SOC) and efficiency, completely changing the approach to energy management strategies and enabling more aggressive downsizing policies without any power availability issues.

Anyway, the SOC itself and its sustainment are crucial aspects that should be carefully analyzed during real driving cycles. The stepwise procedure used in this research makes it possible to confirm the starting hypothesis, providing strong conclusions and evidence of a "backpressure supercompensation effect" associated with rising exhaust backpressure, with acceptable time and computational effort. However, modeling the electrical subsystem, including the battery, converters, and state-of-charge dynamics, as well as the transient response during a real driving cycle, remains a key aspect for verifying compressor boost sustainability in a real case and requires further research, such as the work by Misul in the Finesso et al. study [40]. This type of study represents the next planned step of research and, since the surplus power obtained in pure thermal mode produces indirect benefits, such as extending charge duration and reducing drain, a targeted analysis of the presence of the electric T stage and changes in SOC management could produce effects similar to those already documented in the literature [18].

It is important to note that the limitations of the "backpressure supercompensation effect" appear to be only related to drawbacks at high load and high rotational speed, when the T stage is scaled down beyond a certain limit. The current belief is that these limits could be easily overcome by adopting a strong variable geometry turbine (VGT), whose experimentation will likely be explored further.

The overall results certainly suggest continuing with further investigation into the topic, following the same philosophy, and future research on TGEMS (or similar technologies) aimed at prototype creation.

The results also suggest that the TGEMS research and its possible application to other engine typologies, such as the compression ignition (CI) engine, would produce similar, if not better, performance due to the absence of knock limitations.

5. Conclusions

In this paper, the potential of a novel patented turbo compound layout with supercharging capabilities, the TGEMS system, was assessed for the first time. The new perspective on the ICE, along with the simulation of a 2.0 GDI engine and the T-stage scaling down, led to the discovery of the "backpressure supercompensation effect". While the TGEMS technology initially achieved a -4.92% reduction in specific fuel consumption at 5000 rpm and an +8.75% increase in maximum power output, exploring the limits of this new compensation effect (thanks to the T-stage scaling down combined with operating line control) expanded the maximum specific fuel consumption reductions to -7.93% at 5000 rpm and -6.83% at 3000 rpm, with a maximum power output increase of +11.04%. The results were achieved without electrical power availability issues at steady state.

The available electric power was also maximized, reaching a peak of 21.74 kW through power-split management, which resulted from energy balancing among the turbomachines. Based on the results and their implications, the TGEMS system appears to be a promising candidate for an even more downsized engine in hybrid solutions. Further research into the topic, such as SOC management, CI engine applications, and real driving cycle simulation, has just been planned and is highly recommended. A potential "superbackpressured engine" could open new perspectives, becoming a new reference for mild and full hybrid vehicles.

6. Patents

The reference [25] refers to a patent application currently under secrecy, that is one of the fundamental elements in this research work. It will become publicly accessible once the secrecy period expires and it can be identified with the following information.

- Title: Sistema Turbocompound Elettrico, In Particolare Per Veicoli A Propulsione Ibrida,
- Priority number: 102024000030138,
- Priority date: 30 December 2024,
- Inventor: Andrea Colletto.

Author Contributions: Conceptualization, A.C.; methodology, A.C.; software, A.C.; validation, A.C.; formal analysis, A.C.; investigation, A.C.; resources, A.C., D.A.M. and M.B.; data curation, A.C.; writing—original draft preparation, A.C.; writing—review and editing, A.C., D.A.M. and M.B.; visualization, A.C.; supervision, D.A.M. and M.B.; project administration, A.C. and D.A.M.; funding acquisition, D.A.M. All authors have read and agreed to the published version of the manuscript.

Funding: This research received no external funding.

Data Availability Statement: The original contributions presented in this study are included in the article. Further inquiries can be directed to the corresponding authors.

Conflicts of Interest: The authors declare no conflicts of interest.

Abbreviations

The following abbreviations are used in this manuscript:

Nomenclature

V_d	Unitary displacement
$V_{d,tot}$	Total displacement
B	Bore
S	Stroke
l	Connecting rod length
r_c	Volumetric compression ratio
P_b	Crankshaft brake power
M_b	Crankshaft brake torque
$bmep$	Brake mean effective pressure
$bsfc$	Brake-specific fuel consumption
x_b	Mass fraction burned
a	Efficiency parameter
θ	Crank angle in degrees
θ_0	Start of combustion crank angle in degrees
$\Delta\theta$	Burn duration
m	Wiebe shape function
τ	Ignition delay
β	Pressure ratio
$Temp$	Temperature
N_{red}	Reduced speed
n	Rotational speed
p	Pressure
$\dot{m}_{red}$	Reduced mass flow rate
$\dot{m}$	Mass flow rate
η	Efficiency
$P_{b,tot}$	TGEMS total power unit brake power
P	Power

Subscript

max	Maximum
t	Turbine
c	Compressor
in	Inlet
out	Outlet
el	Electrical
gen	Generator
mot	Motor
f	Fuel

Abbreviations

TC	Turbo compound
M-TC	Mechanical turbo compound
PT	Power turbine
E-TC	Electric turbo compound
eA-TC	Electrically assisted turbo compound
ICE	Internal combustion engine
T	Turbocharger turbine
PU	Power unit
TGEMS	Turbo Generator Electric Multistage Supercharger
CG	Compressor group
GDI	Gasoline direct injection
C	Larger compressor
C'	Smaller compressor
WOT	Wide opening throttle
SI	Spark ignition
SI-Turb	GT-Suite turbulent combustion model
SA	Spark advance
CA50	50% burned crank angle
aTDCf	At top dead center firing
OOL	Optimum operating line
SOC	State of charge
VGT	Variable geometry turbine
CI	Compression ignition

References

1. Arsie, I.; Cricchio, A.; Pianese, C.; Ricciardi, V.; De Cesare, M. Modeling Analysis of Waste Heat Recovery via Thermo-Electric Generator and Electric Turbo-Compound for CO_2 Reduction in Automotive SI Engines. *Energy Procedia* **2015**, *82*, 81–88. [CrossRef]
2. Díaz, S.; Tietge, U.; Dornoff, J.; Mock, P. *CO_2 Emissions from New Passenger Cars in Europe: Car Manufacturers' Performance in 2024*; International Council on Clean Transportation (ICCT): Washington, DC, USA, 2025.
3. Kamo, R.; Bryzik, W. Cummins-TARADCOM Adiabatic Turbocompound Engine Program. *SAE Trans.* **1981**, *90*, 263–274. [CrossRef]
4. Ismail, Y.; Durrieu, D.; Menegazzi, P.; Chesse, P.; Chalet, D. *Potential of Exhaust Heat Recovery by Turbocompounding*; SAE International: Malmö, Sweden, 2012.
5. Salek, F.; Babaie, M.; Ghodsi, A.; Hosseini, S.V.; Zare, A. Energy and Exergy Analysis of a Novel Turbo-Compounding System for Supercharging and Mild Hybridization of a Gasoline Engine. *J. Therm. Anal. Calorim.* **2021**, *145*, 817–828. [CrossRef]
6. Zi, D.; Zhang, L.; Chen, B.; Zhang, Q. Study of the Electric-Booster and Turbo-Generator System and Its Influence on a 1.5 L Gasoline Engine. *Appl. Therm. Eng.* **2019**, *162*, 114236. [CrossRef]
7. Bin Mamat, A.M.I.; Martinez-Botas, R.F.; Rajoo, S.; Romagnoli, A.; Petrovic, S. Waste Heat Recovery Using a Novel High Performance Low Pressure Turbine for Electric Turbocompounding in Downsized Gasoline Engines: Experimental and Computational Analysis. *Energy* **2015**, *90*, 218–234. [CrossRef]
8. Jain, A.; Nueesch, T.; Naegele, C.; Lassus, P.M.; Onder, C.H. Modeling and Control of a Hybrid Electric Vehicle with an Electrically Assisted Turbocharger. *IEEE Trans. Veh. Technol.* **2016**, *65*, 4344–4358. [CrossRef]

9. Repetto, M.; Passalacqua, M.; Vaccaro, L.; Marchesoni, M.; Pini Prato, A. Turbocompound Power Unit Modelling for a Supercapacitor-Based Series Hybrid Vehicle Application. *Energies* **2020**, *13*, 447. [CrossRef]
10. Zhao, R.; Zhuge, W.; Zhang, Y.; Yin, Y.; Zhao, Y.; Chen, Z. Parametric Study of a Turbocompound Diesel Engine Based on an Analytical Model. *Energy* **2016**, *115*, 435–445. [CrossRef]
11. Brancaleoni, P.P.; Corti, E.; Prospero, F.D.; Battista, D.D.; Cipollone, R.; Ravaglioli, V. Optimization of Hydrogen Internal Combustion Engines Equipped with Turbocompound Technology for Enhanced Performance and Efficiency. *Energies* **2025**, *18*, 2166. [CrossRef]
12. Zhao, R.; Zhuge, W.; Zhang, Y.; Yin, Y.; Chen, Z.; Li, Z. Parametric Study of Power Turbine for Diesel Engine Waste Heat Recovery. *Appl. Therm. Eng.* **2014**, *67*, 308–319. [CrossRef]
13. Yong, Y.; Zhijun, W.; Rongchao, Z.; Weilin, Z.; Zongjie, H. Study on Turbocompound System for a Heavy-Duty Diesel Engine by Combining Matching Analysis with Experiments. *Proc. Inst. Mech. Eng. Part D J. Automob. Eng.* **2023**, *237*, 1775–1789. [CrossRef]
14. Dellachà, J.; Damiani, L.; Repetto, M.; Prato, A.P. Dynamic Model for the Energetic Optimization of Turbocompound Hybrid Powertrains. *Energy Procedia* **2014**, *45*, 1047–1056. [CrossRef]
15. Zhuge, W.; Huang, L.; Wei, W.; Zhang, Y.; He, Y. *Optimization of an Electric Turbo Compounding System for Gasoline Engine Exhaust Energy Recovery*; SAE International: Detroit, MI, USA, 2011.
16. Ma, Z.; Zhang, K.; Xiang, H.; Gu, J.; Yang, M.; Deng, K. Experimental Study on Influence of High Exhaust Backpressure on Diesel Engine Performance via Energy and Exergy Analysis. *Energy* **2023**, *263*, 125788. [CrossRef]
17. Zhao, R.; Zhuge, W.; Zhang, Y.; Yang, M.; Martinez-Botas, R.; Yin, Y. Study of Two-Stage Turbine Characteristic and Its Influence on Turbo-Compound Engine Performance. *Energy Convers. Manag.* **2015**, *95*, 414–423. [CrossRef]
18. Briggs, I.; McCullough, G.; Spence, S.; Douglas, R. Whole-Vehicle Modelling of Exhaust Energy Recovery on a Diesel-Electric Hybrid Bus. *Energy* **2014**, *65*, 172–181. [CrossRef]
19. Leng, L.; Yang, X.; Shi, L.; Deng, K. Experimental Investigation of Energy Coupling Mechanism and Regulation Strategies for Turbocompound Engine Efficiency Enhancement. *Energy Convers. Manag.* **2026**, *348*, 120674. [CrossRef]
20. Ferrari, G. *Motori a Combustione Interna*, 2nd ed.; Società Editrice Esculapio: Bologna, Italy, 2016; ISBN 978-88-7488-971-6.
21. Mamat, A.M.I.; Romagnoli, A.; Martinez-Botas, R.F. Characterisation of a Low Pressure Turbine for Turbocompounding Applications in a Heavily Downsized Mild-Hybrid Gasoline Engine. *Energy* **2014**, *64*, 3–16. [CrossRef]
22. Capata, R.; Achille, M. Design and Optimization of Fuel Injection of a 50 kW Micro Turbogas. *Designs* **2018**, *2*, 14. [CrossRef]
23. Kevine Andoh, K.K.; Bademlioglu, A.H. Thermodynamic and Thermoeconomic Analysis of an Intercooled Regenerative Reheat Gas Turbine Cogeneration System: A Case Study for Côte d'Ivoire, West Africa. *Case Stud. Therm. Eng.* **2026**, *80*, 107892. [CrossRef]
24. Zhu, Y.; Yu, Y.; Liu, Y.; He, X.; Xia, G.; Yang, R.; Zhao, S. A Digital Twin Approach for Micro Gas Turbine Performance Based on a Hybrid Model. *Appl. Therm. Eng.* **2026**, *292*, 130279. [CrossRef]
25. Colletto, A. Sistema Turbocompound Elettrico, In Particolare Per Veicoli A Propulsione Ibrida. Patent Priority Number: 102024000030138.
26. Doğan, H.E.; Demirci, A.; Kutlar, A. Estimation of the Shape Factor (m) in Wiebe Function at Different Operating Conditions for a SI Engine. *Int. J. Automot. Eng. Technol.* **2023**, *12*, 75–82. [CrossRef]
27. Lindström, F.; Ångström, H.-E.; Kalghatgi, G.; Möller, C.E. *An Empirical SI Combustion Model Using Laminar Burning Velocity Correlations*; SAE International: Rio de Janeiro, Brazil, 2005.
28. Ghojel, J. Review of the Development and Applications of the Wiebe Function: A Tribute to the Contribution of Ivan Wiebe to Engine Research. *Int. J. Engine Res.* **2010**, *11*, 297. [CrossRef]
29. Kalghatgi, G. Fuel Anti-Knock Quality—Part I, Engine Studies. *SAE Int. J. Fuels Lubr.* **2001**, *110*, 1993–2004. [CrossRef]
30. Grandin, B.; Ångström, H.-E.; Stålhammar, P.; Olofsson, E. *Knock Suppression in a Turbocharged SI Engine by Using Cooled EGR*; SAE International: San Francisco, CA, USA, 1998.
31. Amann, M.; Alger, T.; Mehta, D. The Effect of EGR on Low-Speed Pre-Ignition in Boosted SI Engines. *SAE Int. J. Engines* **2011**, *4*, 235–245. [CrossRef]
32. Millo, F.; Gullino, F.; Rolando, L. Methodological Approach for 1D Simulation of Port Water Injection for Knock Mitigation in a Turbocharged DISI Engine. *Energies* **2020**, *13*, 4297. [CrossRef]
33. Maroteaux, F.; Saad, C.; Aubertin, F. Development and Validation of Double and Single Wiebe Function for Multi-Injection Mode Diesel Engine Combustion Modelling for Hardware-in-the-Loop Applications. *Energy Convers. Manag.* **2015**, *105*, 630–641. [CrossRef]
34. Galindo, J.; Climent, H.; Plá, B.; Jiménez, V.D. Correlations for Wiebe Function Parameters for Combustion Simulation in Two-Stroke Small Engines. *Appl. Therm. Eng.* **2011**, *31*, 1190–1199. [CrossRef]
35. Douaud, A.M.; Eyzat, P. Four-Octane-Number Method for Predicting the Anti-Knock Behavior of Fuels and Engines. *SAE Trans.* **1978**, *87*, 294–308. [CrossRef]

36. Zou, F.; Zeng, H.; Wang, H.; Wang, X.; Xu, Z. Implementation and Parameter Analysis of the Knock Phenomenon of a Marine Dual-Fuel Engine Based on a Two-Zone Combustion Model. *Processes* **2021**, *9*, 602. [CrossRef]
37. Livengood, J.C.; Wu, P.C. Correlation of Autoignition Phenomena in Internal Combustion Engines and Rapid Compression Machines. *Symp. (Int.) Combust.* **1955**, *5*, 347–356. [CrossRef]
38. Baratta, M.; Misul, D. Development of a Method for the Estimation of the Behavior of a CNG Engine over the NEDC Cycle and Its Application to Quantify for the Effect of Hydrogen Addition to Methane Operations. *Fuel* **2015**, *140*, 237–249. [CrossRef]
39. Huang, Y.; Surawski, N.C.; Zhuang, Y.; Zhou, J.L.; Hong, G. Dual Injection: An Effective and Efficient Technology to Use Renewable Fuels in Spark Ignition Engines. *Renew. Sustain. Energy Rev.* **2021**, *143*, 110921. [CrossRef]
40. Finesso, R.; Misul, D.; Spessa, E.; Venditti, M. Optimal Design of Power-Split HEVs Based on Total Cost of Ownership and CO_2 Emission Minimization. *Energies* **2018**, *11*, 1705. [CrossRef]